

“Dissecting” Landscapes with Hölder Exponents to reconcile process and form

Chris J Keylock¹, Arvind Singh², Paola Passalacqua³, and Efi Foufoula-Georgiou⁴

¹Loughborough University

²University of Central Florida

³University of Texas at Austin

⁴University of California, Irvine

November 24, 2022

Abstract

A long-standing question in geomorphology concerns the applicability of statistical models for elevation data based on fractal or multifractal representations of terrain. One difficulty with addressing this question has been the challenge of ascribing statistical significance to metrics adopted to measure landscape properties. In this paper, we use a recently developed surrogate data algorithm to generate synthetic surfaces with identical elevation values as the source dataset, while also preserving the value of the Hölder exponent at any point (the underpinning characteristic of a multifractal surface). Our primary data are from an experimental study of landscape evolution. This allows us to examine how the statistical properties of the surfaces evolve through time and the extent to which they depart from the simple (multi)fractal formalisms. We also study elevation data from Florida and Washington State. We are able to show that the properties of the experimental and actual terrains depart from the simple statistical models. Of particular note is that the number of sub-basins of a given channel order (for orders sufficiently small relative to the basin order) exhibit a clear increase in complexity after a flux steady-state is established in the experimental study. The actual number of basins is much lower than occur in the surrogates. The imprint of diffusive processes on elevation statistics means that, at the very least, a stochastic model for terrain based on a local formalism needs to consider the joint behavior of the elevations and their scaling (as measured by the pointwise Hölder exponents).

Abstract

A long-standing question in geomorphology concerns the applicability of statistical models for elevation data based on fractal or multifractal representations of terrain. One difficulty with addressing this question has been the challenge of ascribing statistical significance to metrics adopted to measure landscape properties. In this paper, we use a recently developed surrogate data algorithm to generate synthetic surfaces with identical elevation values as the source dataset, while also preserving the value of the Hölder exponent at any point (the underpinning characteristic of a multifractal surface). Our primary data are from an experimental study of landscape evolution. This allows us to examine how the statistical properties of the surfaces evolve through time and the extent to which they depart from the simple (multi)fractal formalisms. We also study elevation data from Florida and Washington State. We are able to show that the properties of the experimental and actual terrains depart from the simple statistical models. Of particular note is that the number of sub-basins of a given channel order (for orders sufficiently small relative to the basin order) exhibit a clear increase in complexity after a flux steady-state is established in the experimental study. The actual number of basins is much lower than occur in the surrogates. The imprint of diffusive processes on elevation statistics means that, at the very least, a stochastic model for terrain based on a local formalism needs to consider the joint behavior of the elevations and their scaling (as measured by the pointwise Hölder exponents).

1 Introduction

A landscape is an assemblage of individual, identifiable features that can be classified and explained by the geomorphologist [Arrell *et al.*, 2007; Ehsani and Quiel, 2008; Passalacqua *et al.*, 2010; Clubb *et al.*, 2014], and also the parts in between that are a palimpsest of current and past processes [Jerolmack and Paola, 2010]. A focus on individual landscape features can be key to unlocking the geological history of a region [Gasparini *et al.*, 2014], while consideration of the landscape as a whole using measures such as the hypsometric integral [Strahler, 1952; Boon III and Byrne, 1981; Brocklehurst and Whipple, 2004; Keylock *et al.*, 2020b], or statistical scaling laws topography [Hack, 1957; Tokunaga, 1978; Willgoose, 1994; Lague and Davy, 2003; Zanardo *et al.*, 2013] gives an insight in to how uplift, erosion and deposition interact to shape our landscapes. From the perspective of this latter approach, the question remains as to the extent that statistical models for topography can adequately represent observed elevation statistics. Expressed another way, do the particular dynamics of geomorphic processes leave an imprint on the terrain that makes simple statistical models inadequate? Addressing this question forms the goal of this paper.

The complex configuration and environmental history of a landscape make a formal, mathematical or statistical description of terrain regularity problematic. Attempts to do this have commonly adopted methods based on the notion of fractal dimension [Klinkenberg and Goodchild, 1992; Lifton and Chase, 1992; Outcalt and Melton, 1992; Gagnon *et al.*, 2006]. However, the generalization of the description of landscape from monofractal to one where more than a single fractal dimension is present has resulted in significant terminological confusion. In order to try to resolve this, we propose the definitions given in Table 1. Our table incorporates two commonly adopted descriptions of the statistical scaling of terrain elevations: fractal (here, monofractal) [Klinkenberg and Goodchild, 1992] and multifractal [Lavallée *et al.*, 1993; Gagnon *et al.*, 2006]. Unifying both these descriptions is the principle that a description of elevation statistics may be accomplished in terms of pointwise Hölder regularity [Jaffard, 1997]. This is by far the most common form of regularity used to describe time-series or surface data, although other possibilities exist [Arnéodo *et al.*, 1998; Seuret and Lévy Véhel, 2003]. Monofractality assumes that the Hölder exponent describing the terrain is constant everywhere (it is a Hurst exponent), while multifractality is used in a general sense to mean that the Hölder exponent varies. Here, we use the term “multi-Hölder” rather than “multifractal” for this general no-

85 **Table 1.** Terminology used in this paper concerning the regularity classes and descriptions of topography

Name	Description
Monofractal surface	A surface described effectively by a Hurst exponent. There is no significant difference in the Hölder exponent in space. A fractional Brownian surface with constant Hölder exponent [<i>Mandelbrot and van Ness, 1968</i>].
Multi-Hölder surface	A surface described by multiple Hölder exponents.
Multi-fractional Brownian Surface	A multi-Hölder surface where the variability in Hölder exponent is given by a continuous function as seen with multi-fractional Brownian motion [<i>Peltier and Lévy Véhel, 1995</i>].
Multifractal surface	A multi-Hölder surface where the Hölder exponents are imbricated, leading to either a non-continuous or a random description of their variation.
Conditional multi-Hölder surface	A multi-Hölder surface of either type where the variation in the Hölder exponent exhibits significant association with another variable.
Self-regulating multi-Hölder surface	A special case of a conditional multi-Hölder surface, where the conditioning variable is the elevation. Hence, the statistics of the elevation derivatives are not independent of the elevations [<i>Lévy Véhel, 2013</i>].

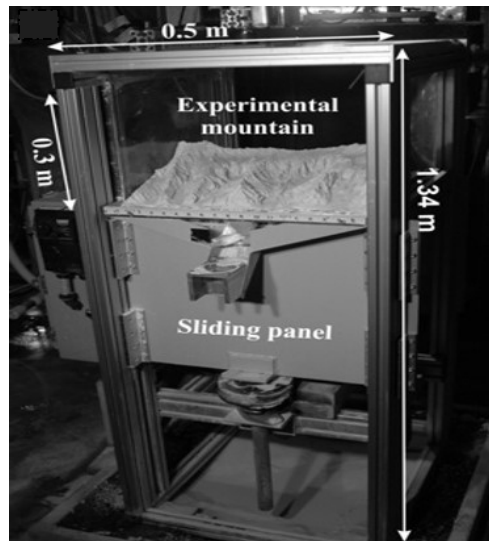
71 tion of a terrain where the Hölder exponents vary. This allows us to contrast a “multifrac-
72 tal” surface with a “multi-fractional Brownian surface” in terms of how the variability is
73 structured. A multifractal surface is one that is the outcome of a hierarchical process such
74 that individual Hölder exponents are imbricated in a non-continuous fashion [*Benzi et al.,*
75 1993], while a multi-fractional Brownian surface is one where the variability is given by
76 a continuous function [*Peltier and Lévy Véhel, 1995*]. Self-regulating processes are rela-
77 tively recent development in regularity theory where the regularity is coupled to the values
78 of the signal [*Echelard et al., 2015*]. This concept underpins the velocity-intermittency
79 method for extracting information on flow structures from turbulence time series [*Key-
80 lock et al., 2012; Ali et al., 2019; Keylock et al., 2020a*]. In addition to this idea of self-
81 regulation, Table 1 also includes the more general category of a “conditional multi-Hölder
82 surface”, where the Hölder exponents are a function of some other terrain property, with
83 the self-regulating process being a special case where this conditioning is on the elevation
84 itself.

86 While previous work has shown that geomorphic surfaces are not monofractal [*Evans*
87 *and McLean, 1995; Perron et al., 2008*], the nature and extent to which a multi-Hölder
88 description of landscape is appropriate is still unclear. While some authors have sug-
89 gested that a multifractal model is suitable [*Gagnon et al., 2006*], others have been more
90 cautious. Of particular importance in this context is a study by *Veneziano and Iacobellis*
91 [1999] that not only critiqued the methodologies adopted in some previous works, but also
92 showed that for various terrains, there was evidence of consistent self-similar relations for
93 both the channel network part of the terrain where fluvial incision was dominant, and the
94 hillslopes dominated by diffusive processes. In other words, landscapes are a conditional
95 multi-Hölder surface, dependent on a categorization into hillslope and channel network.

96 A difficulty with all previous investigations of this phenomenon is the absence of
97 an appropriate control that may be used to compare extracted statistical quantities from
98 topographic surfaces and determine their statistical significance. Given that some of these

99 phenomena are rather subtle in nature, as well as the error in any statistical curve-fitting
 100 exercise used for deriving a scaling relation, this is important. In this study, we develop
 101 a framework that permits analysis of landscape scaling properties relative to appropriate
 102 control models for the topography. We apply this framework to investigate the extent to
 103 which elevation statistics contain a signature from geomorphic processes that cannot be
 104 represented adequately by simple multi-Hölder models for terrain statistics. To accomplish
 105 this, we make use of a laboratory experiment on terrain evolution [*Singh et al.*, 2015], as
 106 well as digital elevation models (DEMs) from Florida and Washington State.

107 2 Experimental set-up



108 **Figure 1.** Illustration of the eXperimental Landscape Evolution (XLE) facility at the University of Min-
 109 nesota.

110 Experiments were performed at the eXperimental Landscape Evolution (XLE) fa-
 111 cility of the St. Anthony Falls Laboratory at the University of Minnesota (Fig. 1). XLE
 112 consisted of a $0.5 \times 0.5 \times 0.3 \text{ m}^3$ erosion box with two opposing sides able to slide up
 113 and down at variable rates mimicking changes in the base level. The facility includes a
 114 rainfall simulator consisting of 20 ultrafine misting nozzles which were able to generate
 115 rain droplets of sizes less than $10 \mu\text{m}$. The experimental setup was also equipped with a
 116 laser scanner able to scan the experimental topography at resolution of 0.5 mm in a few
 117 seconds. This was done every 300 seconds for over nine hours. In this study we report
 118 results in time increments corresponding to this 300 s interval. Thus, $t = 30$ equates to
 119 9,000 seconds. The experimental landscapes discussed here were evolved under constant
 120 uplift, $U = 20 \text{ mm h}^{-1}$, and precipitation intensity, $P = 45 \text{ mm h}^{-1}$. The erodible material
 121 was a homogeneous mixture of fine silica (specific density ~ 2.65) with a grain size distri-
 122 bution of $D_{25} = 10 \mu\text{m}$, $D_{50} = 25 \mu\text{m}$, and $D_{75} = 45 \mu\text{m}$, mixed with 35% water by volume
 123 in a cement mixer; see *Singh et al.* [2015]; *Tejedor et al.* [2017] for more details. The key
 124 changes that arose in the evolution of the topography were the establishment of a drainage
 125 basin at $t \sim 30$ (150 minutes), the main drainage divide at $t \sim 45$ (225 minutes), a steady-
 126 state landscape in terms of sediment flux at $t \sim 75$ (375 minutes), and a final evolution
 127 towards a morphometric steady-state for $t \gtrsim 95$ (475 minutes).

3 Methodology

Previous work has had difficulty discriminating between the various descriptions of terrain provided in Table 1 because of the absence of a suitable testing framework that can permit differences between cases to be assessed with statistical confidence. Thus, to make progress in this field, a new methodology is required. Our formulation of this problem is based on the concept of surrogate data, which have been used for about thirty years for hypothesis testing for non-linear processes in time-series signal processing [Theiler *et al.*, 1992]. This field, including geophysical applications of the salient methods, was recently reviewed by Keylock [2019]. In brief, the most well-known approach is to employ an algorithm that preserves the Fourier amplitudes of a signal and the values of the signal itself, but randomizes the Fourier phases. This is known as the iterated, amplitude adjusted Fourier transform (IAAFT) method [Schreiber and Schmitz, 1996]. Given a linear version of the original signal (i.e. a realization of an autoregressive process), comparison of the original data to the surrogates allows various forms of non-linearity to be detected. In addition, one can determine if the variation in Hölder exponents is sufficient for a signal to be significantly different to monofractal and exhibit statistical intermittency [Poggi *et al.*, 2004; Venema *et al.*, 2006; Basu *et al.*, 2007; Keylock, 2009].

Given the rejection of such a hypothesis of linearity, gradual reconstruction [Keylock, 2010] can then be used to determine how complex a signal is. For example, Keylock *et al.* [2014b] used gradual reconstruction to show how the complexity of river bed topography was a function of discharge, with the superposition of intermediate scale bedforms driving this complexity. Schwenk and Foufoula-Georgiou [2017] used this approach to show that the planform of river meanders encodes information on process nonlinearities, with the behavior of pre-cutoff and post-cutoff meander bends contrasted. Keylock *et al.* [2015] applied this approach to a multi-Hölder model for turbulence and were able to show the statistical significance of relatively small coefficients in a Fokker-Planck model for the velocity increments.

Analysis using surrogate data generated with the IAAFT algorithm is highly suited to distinguishing between mono-fractal signals and any of the class of multi-Hölder signals described in Table 1. However, it cannot be used to discriminate between multi-Hölder surfaces, which is the focus of this study. An algorithm for this class of problem was presented by Keylock [2017] and developed in to a gradual reconstruction framework by Keylock [2018]. Before we describe this technique we briefly review the definition of pointwise Hölder regularity, as this underpins the characterization of the various multi-Hölder surfaces we defined in the introduction.

3.1 Hölder exponents

Given a DEM containing elevations, $z(x, y)$, the increments (the elevation differences between points at separation, r) are:

$$\delta z = z(x, y) - z(x + r \cos \theta, y + r \sin \theta), \quad (1)$$

where θ is a direction selected for analysis and r is the separation distance between points. The statistical moments of order n for δz are given by $\langle |\delta z|^n \rangle$, where the angled braces indicate an averaging operation. The scaling relation

$$\langle |\delta z|^n \rangle \propto r^{\xi_n}, \quad (2)$$

is then found from a log-log plot of $\langle |\delta z|^n \rangle$ against r . A fractal form for the distribution of elevations implies that ξ_n increases linearly with n [Frisch and Parisi, 1985]. In the well-known case of classical turbulence theory, the Kolmogorov [1941] theory gives $\xi_n = \frac{1}{3}n$.

A multi-Hölder signal exhibits a convex relation between n , and ξ_n [Frisch and Parisi, 1985], but is more formally concerned with the set of pointwise Hölder scaling ex-

172 ponents, S_h that characterize the properties of the surface. At a particular position, $z(x =$
 173 $X, y = Y)$ we can evaluate the local scaling behavior of z to determine the Hölder expo-
 174 nent, h , in a fashion that is similar to the statistical moments of the increments, above, but
 175 without the averaging operator:

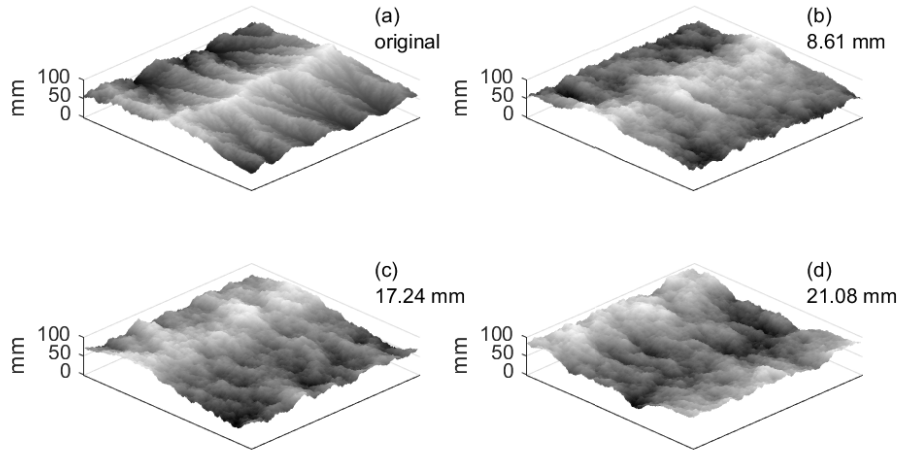
$$|z(X, Y) - Z(X + r\cos\theta, Y + r\sin\theta)| \sim C|r|^{h(x,y)} \quad (3)$$

176 where C is a constant (see *Venugopal et al.* [2006] for a review). Having applied (3) to the
 177 whole DEM, the singularity spectrum, $D(h)$, is given by the set of values for h for which
 178 S_h is not empty. The Frisch-Parisi conjecture states that

$$D(h) = \min_n(hn - \xi_n + 1). \quad (4)$$

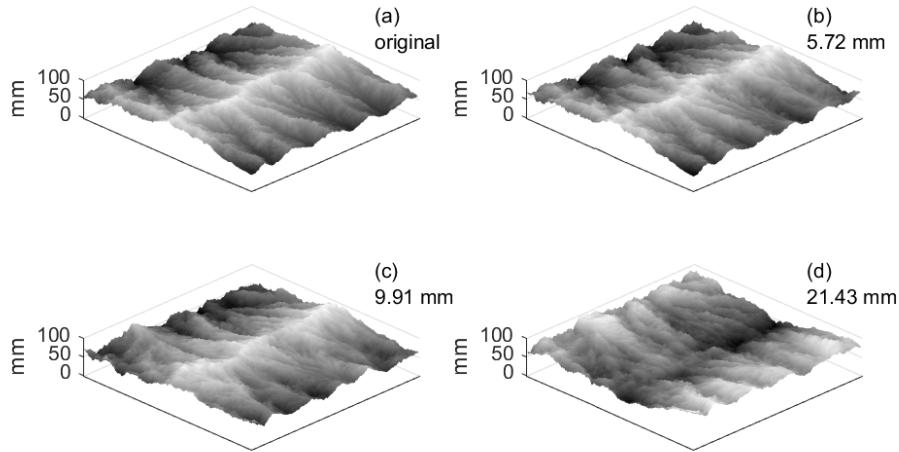
179 Thus, the structure functions and the Hölder exponents are related via a Legendre trans-
 180 form [Jaffard, 1997]. Therefore, a mono-fractal landscape has a constant degree of propor-
 181 tionality between n and ξ_n , giving a single constant value for $D(h)$: the Hurst exponent, d .
 182 The fractal dimension of the surface would then be $\mathcal{D} = 2 + (1 - d)$.

183 3.2 Hypothesis testing with surrogate data



184 **Figure 2.** The original DEM at $t = 100$ is shown in (a), while (b), (c) and (d) show three surrogate DEMs
 185 for this surface generated with the IAAFT algorithm with the minimum, median and maximum root-mean-
 186 squared differences in the elevations, z , of 19 surrogates.

187 Figure 2 shows one DEM from our experiment [*Singh et al.*, 2015], together with
 188 three example surrogates generated by the Fourier amplitude-preserving IAAFT algorithm.
 189 The chosen three DEMs are those with the minimum, median and maximum root-mean-
 190 squared differences in elevation between the surrogate DEM and the original DEM at
 191 $t = 100$. Note that this does not imply one synthetic DEM is better than another; it just
 192 shows the degree of variation intrinsic to the randomization process. The strong visual
 193 contrast between the actual terrain and the surrogates implies straightaway that a mono-
 194 fractal description is inappropriate for describing this surface. This qualitative assessment
 195 may be formalized by generating a total of b surrogate datasets and, assuming a two-tailed
 196 statistical test, if the value for the original data on some measure are greater than or less
 197 than that for all b surrogates, the null hypothesis may be rejected at a significance level of
 198 $\alpha = 2/(b + 1)$, and this is what we do below.

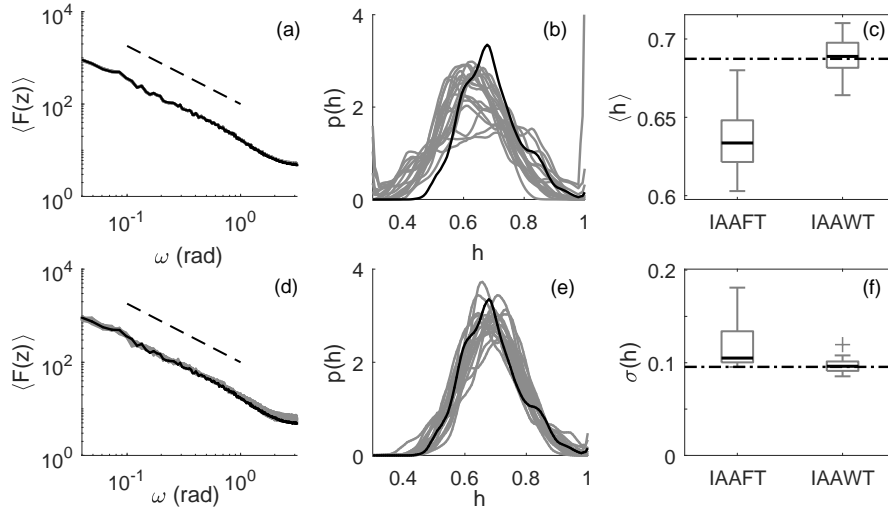


199 **Figure 3.** The original DEM at $t = 100$ is shown in (a), while (b), (c) and (d) show three surrogate DEMs
 200 for this surface generated with the IAAWT algorithm with the minimum, median and maximum root-mean-
 201 squared differences in the elevations, z , of 19 surrogates.

202 Rather than using the IAAFT method, in this study we generate surrogate surfaces
 203 with exactly the same elevation values as the original surface and the same Hölder regu-
 204 larity at a given point in the terrain using the iterated, amplitude adjusted wavelet trans-
 205 form (IAAWT), which was first presented by *Keylock* [2017]. A description of this al-
 206 gorithm and the associated gradual reconstruction methodology is provided in the Ap-
 207 pendix. In brief, the IAAWT algorithm is conceptually similar to the IAAFT algorithm
 208 but replaces Fourier phase-randomization with a wavelet phase-randomization based on
 209 the dual-tree complex-valued wavelet transform [*Kingsbury*, 2001]. As a consequence,
 210 the algorithm produces surrogate data that fix in place the Hölder exponents for the origi-
 211 nal surface, as well as sampling the elevations from the same set of values as contained
 212 in the original DEM. Figure 3 is similar to Fig. 2 but uses the IAAWT as the surface-
 213 generating algorithm. Even though the terrain elevations are randomized (panel (d) has a
 214 valley where the original DEM has its main ridge), it is visually clear that this algorithm
 215 generates much more realistic topographies.

225 The differences between the IAAFT and IAAWT methods are formalized in Fig.
 226 4. The left-most panels show the mean of the absolute part of the Fourier transform of
 227 all 512 horizontal and 512 vertical profiles extracted from the DEM as a function of fre-
 228 quency, ω in radians as a black line, together with the results for the surrogates for the
 229 IAAFT (a) and IAAWT (d) algorithms. A power-law fit is also shown as a dashed line,
 230 indicating that there is ‘mono-fractal-like’ behavior exhibited by these data. Because the
 231 IAAFT algorithm preserves the Fourier amplitudes, not surprisingly there is no visible
 232 difference between data and surrogates on this measure. The IAAWT algorithm also repli-
 233 cates the observed behavior of the Fourier amplitudes to a good level of accuracy but, in
 234 addition, it preserves the multi-Hölder properties as can be seen in the difference in the
 235 histograms for the pointwise Hölder exponents, h in (b) and (e). This is summarized more
 236 effectively by the boxplots in (c) and (f), where the former examines the mean value for h
 237 for data and surrogates, and the latter the standard deviation.

238 Gradual multifractal reconstruction (GMR) introduces a control parameter for the
 239 surrogate data generation, $0 \leq \eta \leq 1$, where $\eta = 0$ equates to surrogates generated by the
 240 IAAWT algorithm (full wavelet phase randomization) and $\eta = 1$ is the original data (no

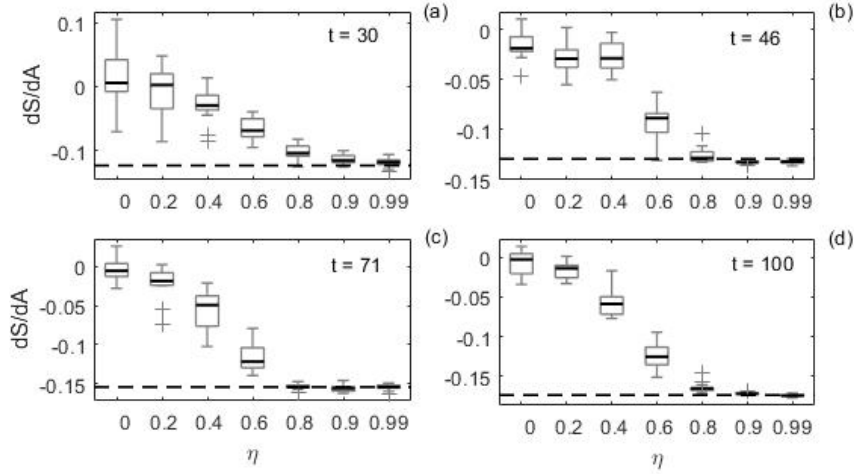


216 **Figure 4.** Statistical properties of the original DEM at $t = 100$ and the surrogate data. Panels (a) and (b)
 217 show results using the IAAFT algorithm and panels (d) and (e) are for the IAAWT algorithm. In each of these
 218 four panels, results for the original data are shown in black and for the surrogates in gray. Panels (a) and (d)
 219 illustrate the spectral properties of the DEMs with a best-fit power-law shown as a dashed line (displaced
 220 vertically). Panels (b) and (e) are the histograms of the pointwise Hölder exponents, h . Panels (c) and (f)
 221 show boxplots of the values of the mean and standard deviation for h , respectively, for nineteen surrogates
 222 DEMs generated with the IAAFT and IAAWT algorithms. The values from the original DEM are shown by
 223 a horizontal dot-dashed line. The box delimits the lower and upper quartiles with the central bar the median.
 224 Whiskers extend for up to 1.5 times the inter-quartile deviation, with outliers shown as crosses.

241 wavelet phase randomization) [Keylock, 2018]. Having selected a value for η , appropriate
 242 surrogates are generated by fixing in place a subset of the wavelet coefficients based on an
 243 energy criterion as described in the Appendix. With this framework it is then possible to
 244 define a threshold value for η , denoted η^* above which there is no significant difference
 245 between data and surrogates. This can be used as a measure of the complexity of the topog-
 246 graphy [Keylock *et al.*, 2014b] and is employed in this study as a way of summarizing
 247 our results.

248 3.3 Geomorphometric measures

249 In this study, we draw upon three basic classes of geomorphometric analysis. The
 250 first is based on the slope-area relation, which Willgoose [1994] showed was highly rele-
 251 vant to the study of evolving topographies with both tectonic and climatological forcing.
 252 The second class utilizes the notion of Horton-Strahler channel ordering to classify sub-
 253 catchments in the DEM into different basin orders, Ω . For all of the basins of a given
 254 order, we then derived the number of basins at that order, $N_B(\Omega)$, and the average total
 255 channel length for a given order, $\langle \sum L(\Omega) \rangle$. Typically, power-law relations for these quan-
 256 tities are found [Rodriguez-Iturbe and Rinaldo, 1997]. However, here we focus on the raw
 257 values rather than the fitted exponent to contrast with the approach taken with slope-area
 258 scaling. These first and second class of geomorphometric measures are similar to those
 259 adopted in related work [Singh *et al.*, 2015; Tejedor *et al.*, 2017]. Our third method is a
 260 recently proposed variant of terrain hypsometry [Strahler, 1952], but modified to include
 261 simultaneous consideration of the Hölder regularity of a landscape [Keylock *et al.*, 2020b].



269 **Figure 5.** Boxplots showing values of dS/dA for the original DEM (horizontal, dashed line) and sur-
 270 rogates (boxplots) as a function of η . The threshold, η^* is obtained by working from right to left until
 271 the last case is found for which there is no significant difference between data and surrogates. This gives
 272 $\eta^* = \{0.8, 0.6, 0.8, 0.9\}$ for $t = 30$, $t = 46$, $t = 71$, and $t = 100$, respectively. The boxplots are formulated in
 273 the same way as in Fig. 4.

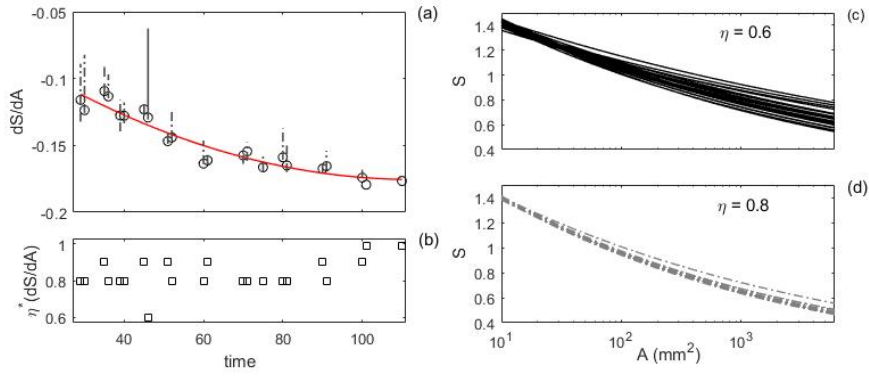
262 For the analysis of the experiment we employed seven η values ($\eta \in \{0.0, 0.2, 0.4, 0.6, 0.8, 0.9, 0.99\}$)
 263 and generated 19 surrogate DEMs for each of twenty-two experimental DEMs using grad-
 264 ual multifractal reconstruction (i.e. 22 original and 2,926 synthetic DEMs were analyzed).
 265 These spanned the times from when the drainage basin was first established at $t \sim 30$,
 266 through the attainment of a flux equilibrium at $t \sim 70$, to beyond the development of a
 267 morphometric steady-state at $t \sim 95$.

268 4 Results

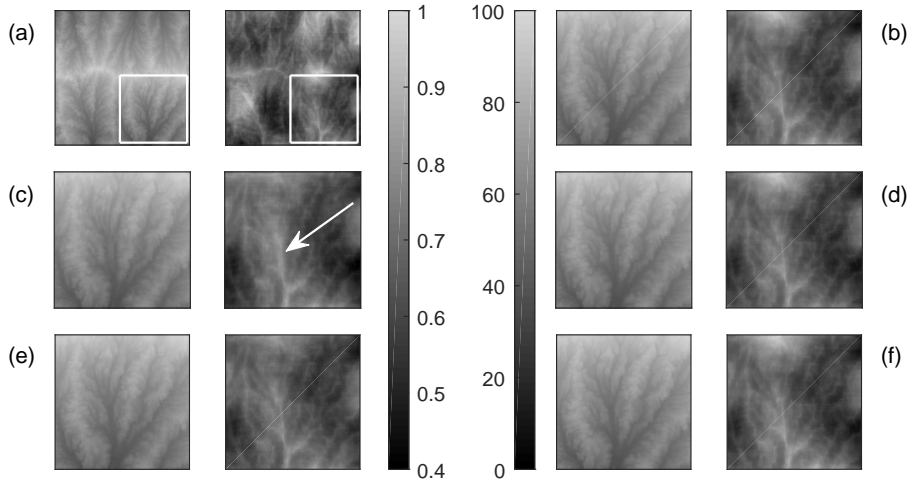
282 4.1 Slope-area relations

283 Figure 5 shows how the threshold values, η^* are determined for the slope-area scal-
 284 ing, dS/dA , for DEMs obtained at four instances that span the experimental duration. All
 285 DEMs clearly have values for dS/dA that depart from those obtained from a simple multi-
 286 Hölder representation of the terrain at $\eta = 0$. Once the central drainage divide is estab-
 287 lished in the experiment, i.e. for $t \gtrsim 30$, the surrogate landscapes differ from the actual
 288 DEM for $\eta \leq 0.4$. With 19 surrogates generated and a directional, one-tailed hypothesis
 289 that dS/dA for the surrogates is not significantly greater than for the original DEM, our
 290 analysis indicates a significant difference at the 5% level up to $\eta = 0.8$ for most cases.

291 Given values for $\eta^*(dS/dA)$ for all 22 DEMs, Fig. 6b shows how these vary as a
 292 function of the evolution of the catchment. All values are high and there is a possible
 293 weak tendency in these results with random variability in the range $0.6 < \eta^*(dS/dA) \leq 0.9$
 294 up until a flux equilibrium is established at $t \sim 70$, followed by a gradual increase in
 295 $\eta^*(dS/dA)$ beyond this point. Figure 6a shows the values for dS/dA as a function of time,
 296 with a quadratic decay illustrated by a red line. The vertical lines extending from each
 297 symbol show a form of confidence interval that is possible using surrogate data analysis
 298 [Keylock, 2012]; one based on the range of values for the surrogates at the appropriate
 299 $\eta^*(t)$, rather than quality of fit to one set of data. It is clear that: (a) the one instance of
 300 $\eta^*(dS/dA) = 0.6$, at $t = 45$, is a consequence of a great range to the fitted slopes at this
 301 time; and, (b) the change in dS/dA with time is significant.



274 **Figure 6.** The slope-area scaling exponent as a function of the DEM number (time, t) is shown in panel (a)
 275 as a circle, with a best-fit quadratic as a red curve. The vertical dark gray lines show the range of values for
 276 the gradual multifractal reconstruction (GMR) surrogates at the value for $\eta^*(dS/dA)$, with $\eta^*(dS/dA) = 0.6$
 277 (solid), $\eta^*(dS/dA) = 0.8$ (dash-dotted), and $\eta^*(dS/dA) = 0.9$ (dashed). The variation for $\eta^*(dS/dA) = 0.99$
 278 is little greater than the size of the circles. Panel (b) shows these values for $\eta^*(dS/dA)$ as a function of time.
 279 Panels (c) and (d) show the relation between basin slope and upstream contributing area for the surrogate data
 280 at $t = 100$ for $\eta = 0.6$ (c) and $\eta = 0.8$ (d). Results are shown on semi-logarithmic axes for clarity, although all
 281 fits are of a power-law form.



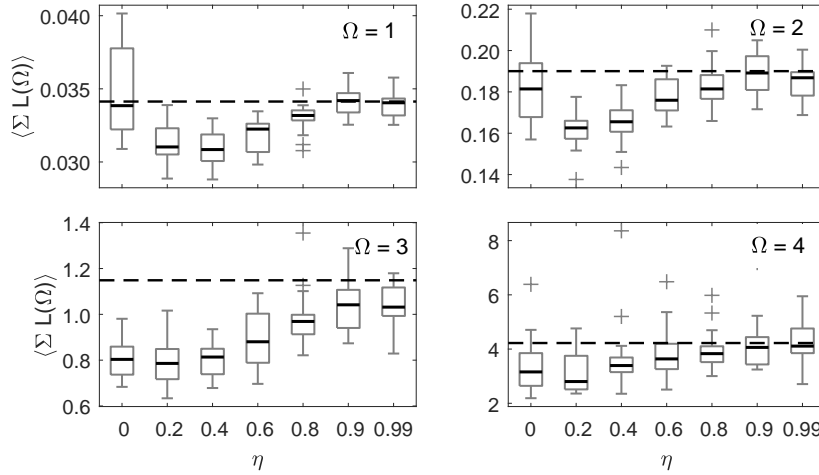
302 **Figure 7.** The DEM extracted at $t = 100$ in plan view, together with accompanying surrogate data. In each
 303 of six cases, two panels are shown with the left-hand cases illustrating the elevations, z , and the right-hand
 304 the Hölder exponents. Panel (a) is the original DEM with a white box showing the region extracted in the
 305 other panels. Panel (b) is this extracted region, (c) is the surrogate DEM at $\eta = 0.6$ with the median value
 306 for dS/dA , while (d), (e) and (f) are the surrogate DEMs at $\eta = 0.8$ with the median value, maximum and
 307 minimum values for dS/dA , respectively. The arrow highlights a feature discussed in the text.

308 In order to understand why the $\eta^*(dS/dA)$ values are generally high, in Fig. 6c and
 309 d we plot the fitted power-laws for the surrogates using the DEM for $t = 100$ as an exam-

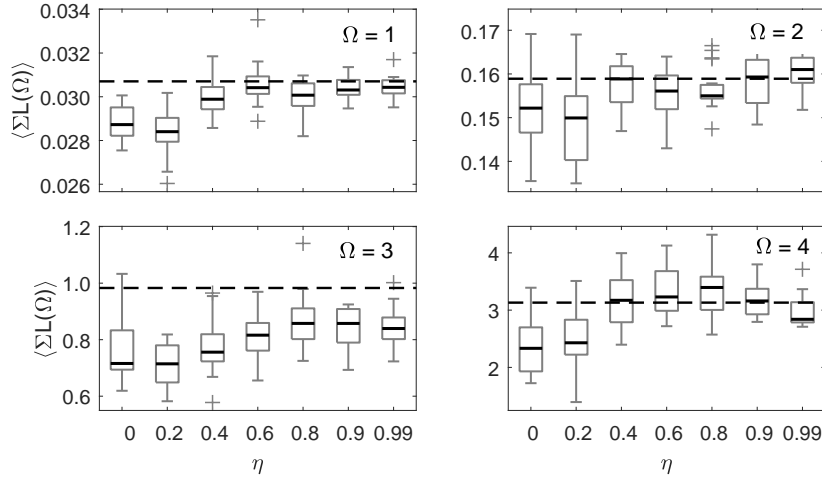
310 ple. For $\eta = 0.6$ and $\eta = 0.8$ the slopes for the small area basins are the same (~ 1.4),
 311 while they are significantly lower for the large basins at $\eta = 0.8$. Hence, we can explain
 312 why the surrogates cannot replicate the dS/dA values at low η : the slopes of the larger
 313 basins are too steep. As small basins are typically located in the headwater catchments,
 314 the true landscape has a stronger coupling between lower elevations and reduced gradi-
 315 ents, implying some degree of self-regulation as defined in Table 1, and as considered
 316 in section 5. Thus, the shortcomings of a simple multi-Hölder model are less in the rep-
 317 resentation of the dissected, upper basins but rather in the correct representation of the
 318 deposition-dominated, larger catchments.

319 To illustrate the difficulty of detecting these differences by observation and, thus, the
 320 difficulty of evaluating the verisimilitude of a multi-Hölder model by qualitative assess-
 321 ment, we show in Fig. 7 the detail of the original data and various surrogate DEMs for
 322 $t = 100$. Panel (a) shows a plan view of the original DEM, while panel (b) highlights the
 323 region in the white box in panel (a). From Fig. 5d, the surrogate DEM at $\eta = 0.6$ with the
 324 median value for dS/dA and that at $\eta = 0.8$ with the maximum for dS/dA shown in pan-
 325 els (c) and (e), respectively, are in error, while the surrogate at $\eta = 0.8$ with the median
 326 and minimum for dS/dA shown in (d) and (f), respectively, are very close to the original
 327 case. The highlighted area of the DEM is one containing a large basin consisting of low
 328 elevations and high values for h . The primary visible difference is that the spine of high
 329 h values in (c) indicated by the arrow is too broad and diffuse relative to the cases seen
 330 in panels (b), (d) and (f). This results in high h values being associated with somewhat
 331 higher z values than in the original DEM, causing reduced values for dS/dA at $\eta = 0.6$
 332 compared to the true case. Clearly, a surrogate data framework is needed to extract such
 333 subtleties with statistical confidence.

334 4.2 Average total channel length



335 **Figure 8.** Boxplots showing the determination of $\eta^*(L)$ for the DEM at $t = 30$ for basin orders
 336 $\Omega \in \{1, 2, 3, 4\}$. The values of $\langle \sum L(\Omega) \rangle$ for the surrogates are shown as boxplots a function of η , with the
 337 dashed lines showing the value for the data itself. From these plots, $\eta^*(L) = \{0.8, 0.6, 0.8, 0.0\}$ for ascending
 338 values of Ω . The boxplots are formulated in the same way as in Fig. 4.

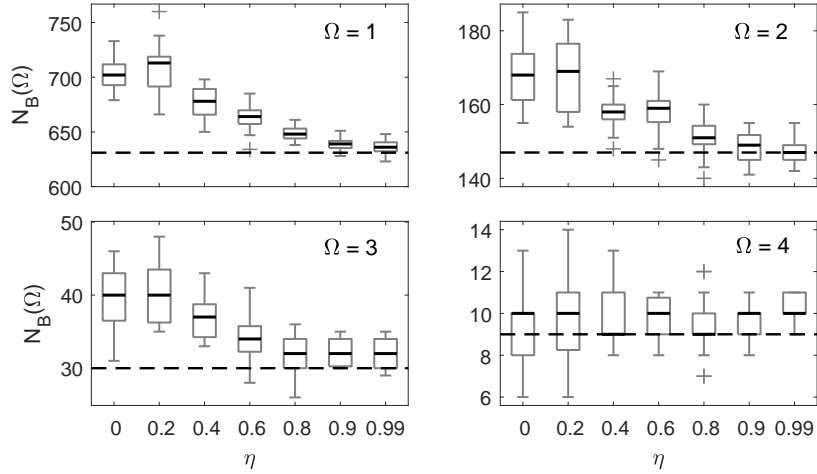


339 **Figure 9.** Boxplots showing the determination of $\eta^*(L)$ for the DEM at $t = 100$ for basin orders
 340 $\Omega \in \{1, 2, 3, 4\}$. The values of $\langle \sum L(\Omega) \rangle$ for the surrogates are shown as a function of η , with the dashed
 341 lines showing the value for the data itself. From these plots, $\eta^*(L) = \{0.4, 0.0, 0.99, 0.0\}$ for ascending values
 342 of Ω . The boxplots are formulated in the same way as in Fig. 4.

343 Figures 8 and 9 show the average channel length for basins of four Horton-Strahler
 344 orders at two different times as a function of η . These results contrast with the slope-area
 345 scaling as a simple multi-Hölder model with no additional constraints ($\eta = 0$) can repli-
 346 cate the observed channel lengths in many cases, even though η^* itself is often greater.
 347 Furthermore, in neither case do the fourth order basins indicate any significant differences.
 348 These are the largest in the system and are integrating information over a sufficiently large
 349 area that the preservation of the elevations and the approximate preservation of the h is
 350 sufficient to get the average channel length statistics correct. However, at $t = 30$ and before
 351 the drainage divide is firmly established, the values of $\langle \sum L(\Omega) \rangle$ for $\Omega = 3$ are a sensi-
 352 tive measure, implying that the properties of third order basins are highly dependent on
 353 the structure of the main divide. While η^* is also high for $\Omega = 3$ for $t = 100$, the $\eta = 0$
 354 case can attain the requisite values by chance. In contrast, in this case, it is the $\Omega = 1$
 355 basins where additional structure is required to get the correct channel length statistics,
 356 with the surrogates producing lengths that are too short. The implication of the slopes be-
 357 ing matched very well for small basins at $t = 100$ (Fig. 6c) but $\langle \sum L(\Omega = 1) \rangle$ being too
 358 small is that a simple multi-Hölder model cannot adequately represent either basin shape
 359 or valley sinuosity effects correctly.

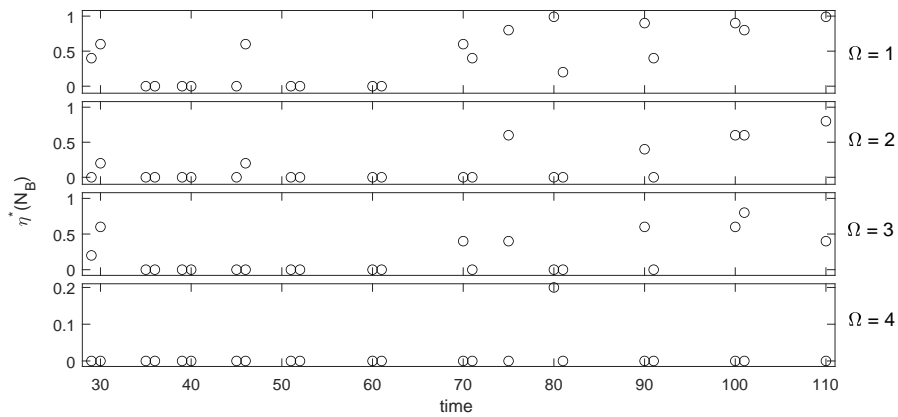
360 4.3 Total number of basins

365 Three classical scalings for drainage basins as a function of stream order are the
 366 laws of stream number, stream length and basin area [Rodriguez-Iturbe and Rinaldo,
 367 1997]. Because we found that the behavior for basin area was similar to that for stream
 368 length, we do not report those results here, focusing instead on the stream number results,
 369 which in terms of our analysis we state as the number of basins of a given order, $N_B(\Omega)$
 370 and present the results for $t = 100$ in Fig. 10. Here a much stronger effect was found in
 371 terms of significant differences at $\eta = 0$ for different stream orders less than $\Omega = 4$. Thus,
 372 $N_B(\Omega)$ is a more sensitive metric than $\langle \sum L(\Omega) \rangle$ for studying landscape complexity. In
 373 Fig. 11 we plot $\eta^*(N_B)$ for all four stream orders as a function of time. As with the re-
 374 sults for dS/dA in Fig. 6b, a transition seems to emerge after about $t = 70$, but the effect
 375 is much more marked here: complexity measured by η^* really only increases once the flux

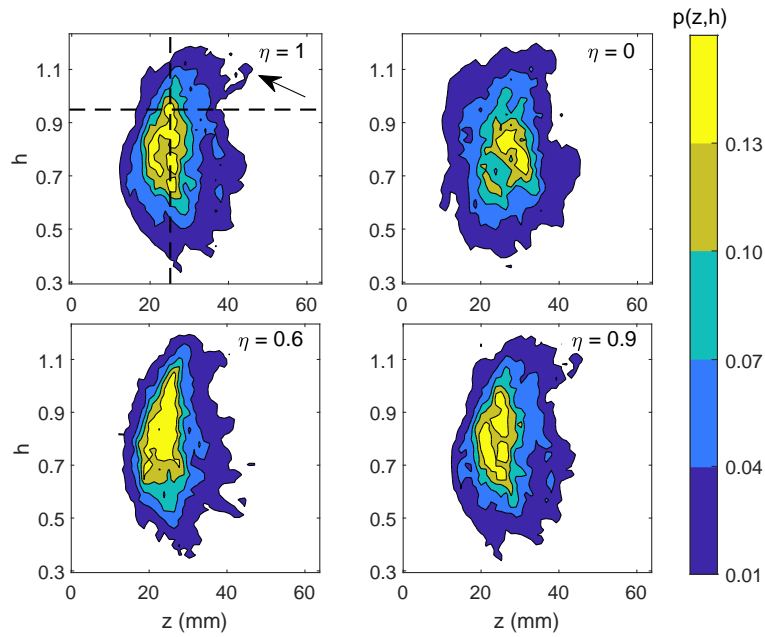


361 **Figure 10.** Boxplots showing the determination of $\eta^*(N_B)$ for the DEM at $t = 100$ for different basin or-
 362 ders, Ω . The values of N_B for the surrogates are shown as a function of η in each panel, with the dashed lines
 363 showing the value for the data itself. From these plots, $\eta^*(N_B) = \{0.9, 0.6, 0.6, 0.0\}$ for stream orders, 1 to 4,
 364 respectively. The boxplots are formulated in the same way as in Fig. 4.

376 steady-state is established for $t > 70$; it is only in the early stages of landscape that a simple
 377 multi-Hölder model is effective. Given that flux steady state was defined as the condi-
 378 tion where the erosional fluxes balanced out the sediment provided by the rock uplift and
 379 was obtained by direct measurement during the experiment [Singh *et al.*, 2015], the congru-
 380 ence between the attainment of this state and the increase in η^* is rather remarkable.
 381 The implication is that complexity increases once diffusive forces gain greater prominence
 382 in the landscape dynamics.

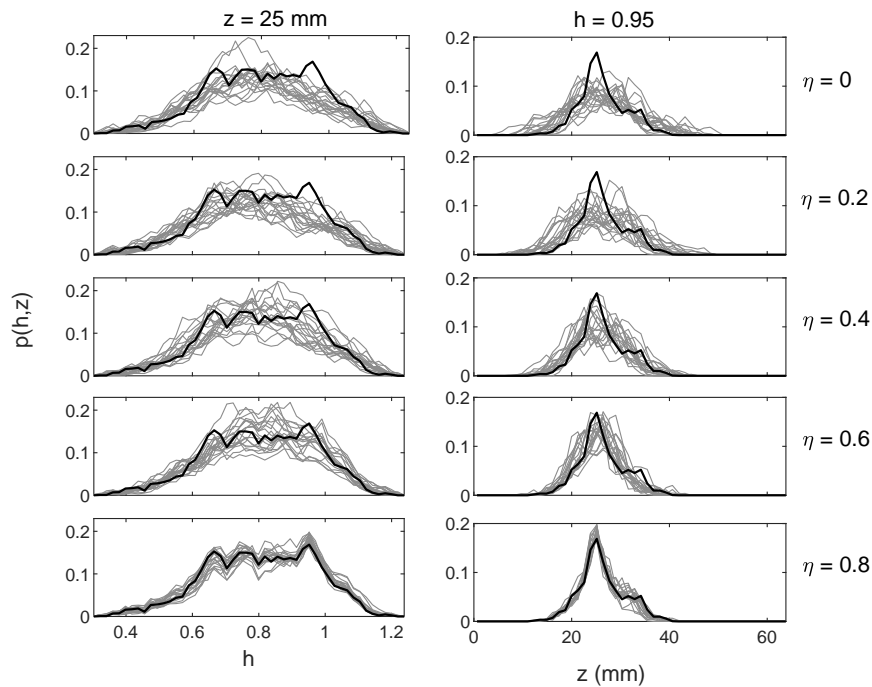


383 **Figure 11.** Values for $\eta^*(N_B)$ as a function of stream order, Ω (each panel) and time.



385 **Figure 12.** Probability contours for the joint distributions of the elevations, z , and Hölder exponents, h , for
 386 the DEM obtained at $t = 100$ for the original data (a) and three surrogate datasets at the value for η stated
 387 in each panel. Each surrogate DEM shown is that with the median RMSE between data and surrogates for
 388 the joint PDF. The dashed construction lines in panel (a) are the transects examined in Fig. 13 and the arrow
 389 identifies a feature discussed in the text.

384 5 The joint distribution of elevation and regularity



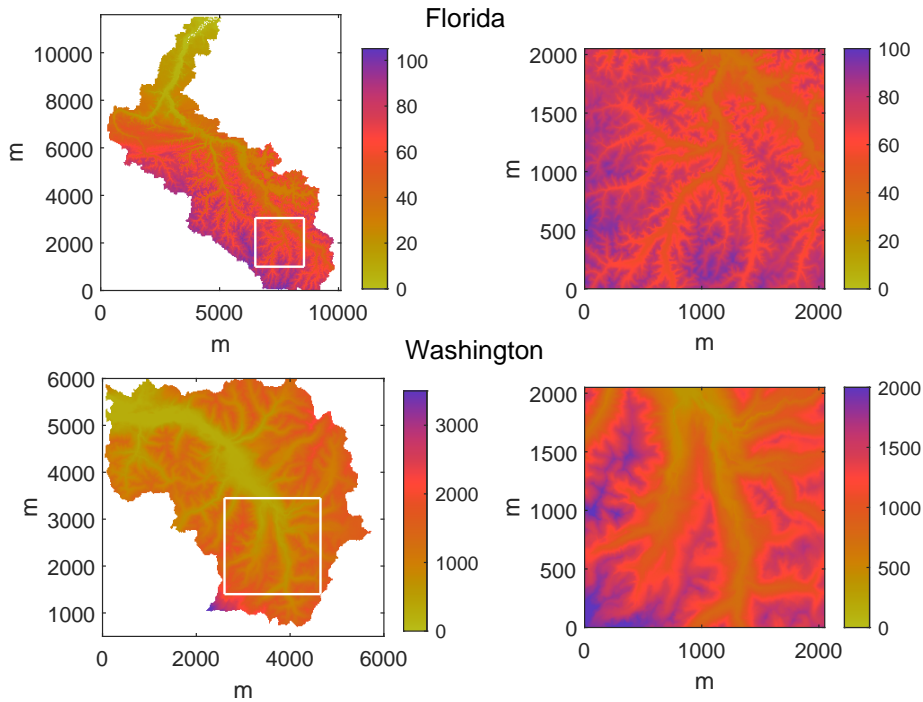
390 **Figure 13.** Transects through the joint PDF shown in Fig. 12a are shown in each panel as a solid line,
 391 together with the transects for nineteen surrogates at the stated value for η . The left-hand column of panels
 392 show the transect, $p(h|z = 25 \text{ mm})$, i.e. the vertical line in Fig. 12a, while the right-hand column is for the
 393 horizontal line in Fig. 12a, i.e. $p(z|h = 0.95)$. The conditional distributions shown are not renormalized; they
 394 are transects through the joint PDF.

395 A recent extension to the classic hypsometry measure of *Strahler* [1952] examines
 396 the joint probability distribution function (PDF) between the elevations, z and the Hölder
 397 exponents, h [Keylock *et al.*, 2020b]. In other words, it captures the coupling that under-
 398 pins the nature of a self-regulating landscape as defined in Table 1. The top-left panel
 399 of Fig. 12 shows this PDF for the original DEM at $t = 100$. The other panels show the
 400 results for the surrogate DEM with the median RMSE for different choices of η . Recall
 401 that our algorithm uses exactly the same z values. Hence, there is no difference in the
 402 marginal distribution for z and the hypsometries for all of these data are identical. How-
 403 ever, there are clear differences in the shape of the joint PDFs and, as η increases, rel-
 404 atively subtle features of the original PDF, such as the outlying region identified by the
 405 arrow in the top-left panel, begin to be captured in the surrogates. Here we focus on two
 406 conditional distributions given by the transects through the joint distribution shown by
 407 the dashed lines in the upper left panel. These pass through the mode of the distribution
 408 at $z = 25$ mm, $h = 0.95$ and are given by the black line in each panel of Fig. 13. The
 409 gray lines in this figure are the equivalent conditional distributions for the surrogates at
 410 the stated value for η . It is clear that at low η , the surrogate data cannot replicate this
 411 mode, which is too large in magnitude for $p(z|h = 0.95)$ given in the right-hand col-
 412 umn and is located at too high a value for h for $p(h|z = 25)$ in the left-hand column. A
 413 threshold value of $\eta^* = 0.4$ is appropriate from this analysis. Hence, once more, a simple
 414 multi-Hölder model cannot serve, and the key difficulty for such a model in terms of self-
 415 regulation is to have a sufficient number of intermediate elevations that are as smooth as
 416 $h = 0.95$.

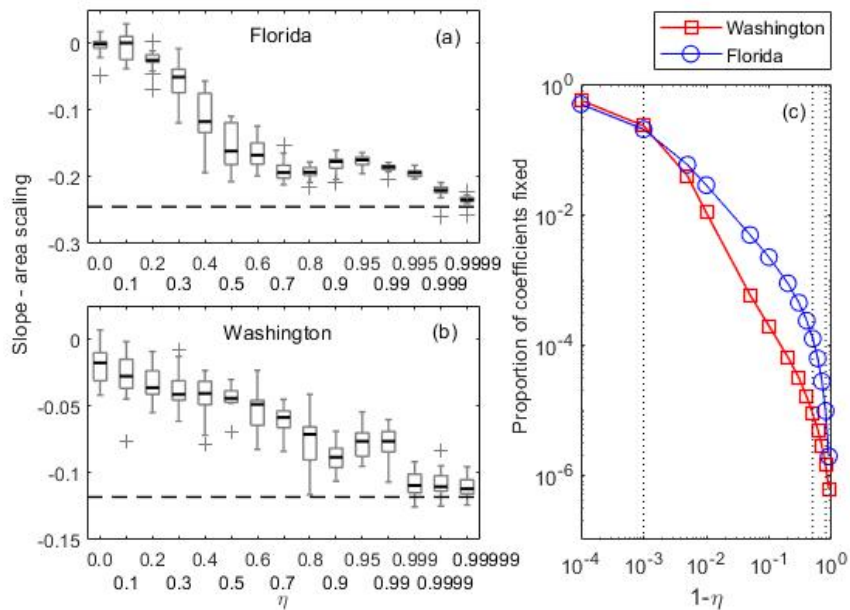
417 Physically, this means that diffusive processes, which increase h at intermediate ele-
 418 vations, gain in geomorphic significance once the landscape attains a flux equilibrium, and
 419 are more important to the landscape structure than a simple multi-Hölder model can cap-
 420 ture. This result is consistent with the earlier results that the simple multi-Hölder model
 421 produces too many basins of a given order (incision is excessive relative to diffusion) and
 422 has slopes that are over-steepened within the largest basins. Significant diffusive action on
 423 the intermediate slopes will result in fewer basins of intermediate order and will promote
 424 a reduction in average slopes for the larger watersheds of which these slopes are a part.

425 6 Application to two distinct topographies

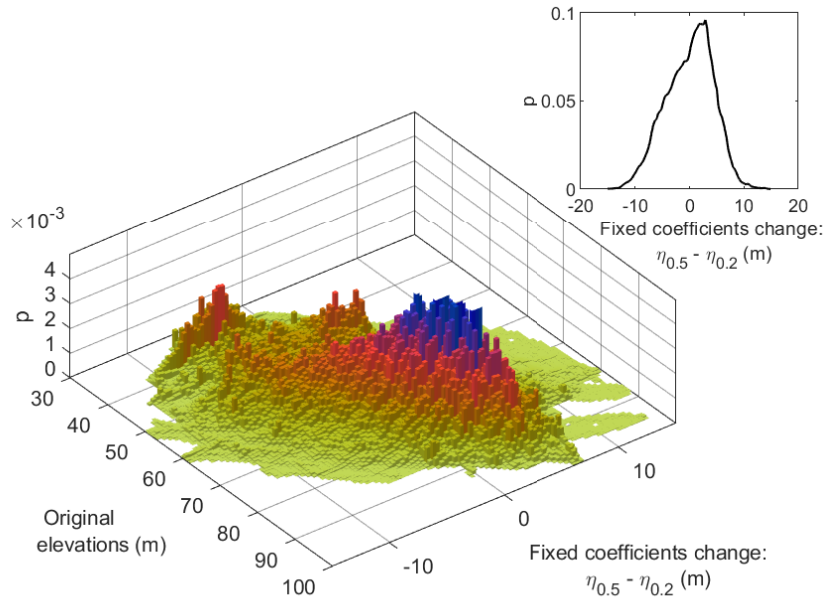
429 While the experimental surfaces allow us to examine the evolution of a topography's
 430 response to a particular forcing, the idealized boundary conditions mean that there is not
 431 necessarily a relation to any specific observed terrain. As a consequence, in this section
 432 of the paper we examine the geomorphometry of two contrasting regions of the conter-
 433 minous United States, Florida and Washington State, focusing on the slope-area scaling
 434 properties. The two DEMs were obtained from the USGS National Elevation Dataset at
 435 <https://catalog.data.gov/dataset/usgs-national-elevation-dataset-ned> and both cover an area
 436 of 20.48×20.48 km at a $1/3$ arc-second (10 m) resolution. The particular drainage basins
 437 are the Ochlockonee River basin in Florida and the Cowlitz River basin in Washington
 438 State and these are shown in Fig. 14. The elevation range in the former is 0.5 m to 105
 439 m, and is 263 m to 4100 m in the latter, while in the extracted regions, elevation ranges
 440 from 33.3 m to 100.8 m for the Florida case, and 361 m to 2274 m for the Washington
 441 case.



426 **Figure 14.** The two drainage basins from Florida (upper) and Washington State (lower) are shown in the
 427 left-hand panels, with the 2048×2048 m sub-regions that are analyzed in detail highlighted in the right-hand
 428 panels. The colorbars show the elevation range (m) in each panel.



442 **Figure 15.** Values for the slope-area scaling exponent for the surrogate data as a function of η for Florida
 443 (a) and Washington (b), with the actual value shown as a horizontal, dashed line. Panel (c) shows the propor-
 444 tion of fixed wavelet coefficients as a function of $1 - \eta$ for the Washington and Florida DEMs. Vertical dotted
 445 lines highlight the values at, from left to right, $\eta = 0.999$, $\eta = 0.5$, $\eta = 0.2$ as discussed in the text.



446 **Figure 16.** The joint probability distribution function of the difference in elevations between the DEMs
 447 reconstructed from the fixed wavelet coefficients at $\eta = 0.5$ and $\eta = 0.2$ versus the elevations in the original
 448 DEM. The marginal distribution for the former variable is shown in the inset panel.

449 Panels (a) and (b) in Fig. 15 show that the slope-area scaling for these two topographies
 450 is significantly different, with the scaling exponent nearly double in magnitude for
 451 the Florida case. Despite this difference, both basins have $\eta^* = 0.999$, although while
 452 the surrogates for the Washington DEM have a slope-area scaling exponent that converges
 453 on the true values in an approximately linear fashion, the Florida data exhibit a rapid
 454 decrease in the value of dS/dA for $0.2 < \eta \leq 0.5$ and a small increase for $0.8 < \eta \leq 0.95$.
 455 To investigate this further we examined the fixed wavelet coefficients at these choices for
 456 η . The proportion of fixed coefficients as a function of η is given in Fig. 15c. It is notable
 457 that for both DEMs, $\eta = 0.999$ equates to about 20% of the coefficients being fixed, but
 458 that for lower values for η (to the right in this panel) there is a clear divergence in the pro-
 459 portion of coefficients fixed between the two DEMs, with energy spread among a greater
 460 number of coefficients for the Florida case. We reconstructed the Florida DEM from the
 461 fixed coefficients at $\eta = 0.2$ and $\eta = 0.5$, and then found the difference between these
 462 DEMs. Thus, we examined how the topography fixed in place in the algorithm changed
 463 over this range of values for η . The inset in Fig. 16 shows the histogram of the elevation
 464 change between these two DEMs formed from the fixed coefficients. Clearly, the typical
 465 change is an increase by 5 m to the DEM elevations from $\eta = 0.2$ to $\eta = 0.5$. The main
 466 panel of Fig. 16 shows the joint PDF of the change in the elevations against the elevations
 467 in the original DEM. The modal change of +5m is concentrated between 60m and 80m
 468 although there are also two other modes: an incision mode where the elevation change is
 469 ~ -5 m, concentrated in the lowest elevations (≤ 40 m), and another constructive mode
 470 where the elevation increases by ~ 5 m at low elevation (45 m). Consequently, we can con-
 471 clude that the key difficulty for a multi-Hölder model in replicating the slope-area scaling
 472 for the Florida case-study is in allocating sufficient heights to these intermediate eleva-
 473 tions. In other words, these regions in the terrain are dissected too much in the low η sur-
 474 rogates, while in nature the greater preponderance of diffusive processes preserves these
 475 elevations. This is consistent with the earlier analysis of the number of $\Omega = 1$ basins and
 476 of the slope-area scaling for the experimental surfaces. Preserving mass in the topography

477 in the 60m-80m elevation range at $\eta = 0.5$ results in greater slopes in the smaller area
 478 basins, changing the median slope-area scaling for the surrogates from -0.026 for $\eta = 0.2$
 479 to -0.162 at $\eta = 0.5$.

480 7 Conclusion

481 In this paper we have formalized the nonlinear analysis of digital elevation models
 482 using the gradual multifractal reconstruction (GMR) framework. In particular, we have
 483 used experimental, evolving landscapes to show that a simple multi-Hölder model for ter-
 484 rain, even with the set of elevations, z , constrained to the original values and the pointwise
 485 Hölder exponents located correctly in the terrain, is not sufficient to replicate several mea-
 486 sures of geomorphometry. Our analysis framework has shown that the slope-area scaling
 487 relation, dS/dA and, particularly, the number of basins for a given Horton-Strahler stream
 488 order (when this is less than the scale of the system studied) are sensitive measures of
 489 landscape structure. The slope-area scaling was also applied to regions of the same area
 490 from Florida and Washington State with an order of magnitude difference in elevation
 491 range. Despite very different values for dS/dA , the values for the GMR control parameter
 492 at which there was no significant difference between data and surrogates was very similar
 493 ($\eta^* = 0.999$) and very different to the value of $\eta^* = 0$ expected if a simple multi-Hölder or
 494 multifractal model is sufficient to describe the topography.

495 What was particularly notable in our experimental results was that once the land-
 496 scape attained an equilibrium in terms of flux, the morphology was still evolving, and
 497 becoming more complex according to our significance testing framework. Indeed, it was
 498 only once this flux equilibrium was established that such an effect was clear. This was as-
 499 sociated with the relative preponderance of diffusive phenomena such that, when a topog-
 500 raphy is in the early stages of evolving from a perturbation, a simple multi-Hölder stochas-
 501 tic process may be able to replicate most geomorphically relevant measures of landscape
 502 structure. However, when changes in flux become negligible, it is the subtle re-working of
 503 a landscape by more diffusive processes that results in an increase in landscape complex-
 504 ity as measured by η^* . This was particularly associated with the coupling between low or
 505 intermediate elevations and large Hölder exponents (smooth regions).

506 Our observations raise the question of which class of stochastic processes provides
 507 a potential guide to modeling mature landscape surfaces effectively. Our results in Figs.
 508 12 and 13 are explicitly about the coupling between the Hölder exponents and the ele-
 509 vations themselves and that they demonstrate an association implies that self-regulating
 510 multi-Hölder surfaces [Lévy Véhel, 2013; Echelard *et al.*, 2015] may have some potential.
 511 It also lends support to the recent suggestion that hypsometric analysis can be usefully ex-
 512 tended by simultaneous consideration of elevation and Hölder regularity [Keylock *et al.*,
 513 2020b]. However, our results also reveal no simple relation between elevation and Hölder
 514 regularity, implying further conditioning is necessary as alluded to in Table 1. As noted in
 515 the introduction, Veneziano and Iacobellis [1999] proposed that differing Hölder regularity
 516 could be associated with the channel network and the hillslope and their hypothesis may
 517 have some potential based on our analysis. However, such an approach takes us full circle
 518 as the introduction began by contrasting geomorphic studies that focus on extracted land-
 519 scape features with those that attempt to characterize the landscape as a whole, with the
 520 latter philosophy guiding the work presented here. Advances in digital terrain processing,
 521 [e.g. Passalacqua *et al.*, 2010], simplify the process of DEM classification and the next
 522 stage of our work is to form a set of landscape regimes and determine the Hölder condi-
 523 tioning for each, potentially also as a function of elevation. This will lead to a means
 524 to determine a statistical modeling framework for natural terrains. The hypothesis testing
 525 framework introduced here, or one similar in nature, will be needed to examine the func-
 526 tional relations between landscape regimes and Hölder regularity and, thus, the statistical
 527 significance of particular landscape regimes for such a model.

A: The IAAWT algorithm and gradual reconstruction

The IAAWT algorithm is based on a dual-tree complex wavelet transform (DTCWT) [Kingsbury, 2001; Selesnick et al., 2005]. A pair of dyadic wavelet trees may be constructed to form a Hilbert pair [Selesnick, 2002], resulting in a complex transform. This can be achieved for orthogonal wavelets by offsetting the scaling filters by one half sample. The naïve approach would then be to deploy two trees of linear phase filters, of even length in one tree and odd in the other. However, such filters lack orthogonality and the sub-sampling structure is not particularly symmetric. Thus, Kingsbury [2001] formulated the *Q-shift* dual tree where, below the coarsest scale, all filters are even length, but no longer linear in phase. By designing the filters to have a delay of $\frac{1}{4}$ sample and by using the time reverse of one set of filters in the other tree, the required $\frac{1}{2}$ sample delay can be achieved. In this paper we use symmetric, biorthogonal filters with support widths of 13 and 19 values for the first level of the algorithm and *Q-shift* filters with a support of 14 values for all other levels on the dual tree (case C in Kingsbury [2001]). The *Q-shift* dual tree approach retains properties that make undecimated transforms advantageous for use in surrogate generation, such as shift invariance, but at a computational cost that is merely double that for a standard discrete wavelet transform. In addition, although we do not use it in this study, the transform also has enhanced directional selectivity compared to a classic discrete wavelet transform.

The IAAWT algorithm for a DEM containing elevations, $z(x, y)$, where $x = y = 2^J$, and where J is an integer, proceeds as follows:

1. Store the original elevations $z(x, y)$;
2. Apply the two-dimensional DTCWT and obtain wavelet amplitudes, $A_{k,\ell,j,p}$ and wavelet phases, $\omega_{k,\ell,j,p}$ over all $j = 1, \dots, J$ scales for the $p = 1, \dots, 6$ planes at each scale and for wavelet coefficient, w , with coordinates, (k, ℓ) , where at each j there are $6 \times 2^{2(J-j)}$ coefficients:

$$\begin{aligned} A_{k,\ell,j,p} &= |w_{k,\ell,j,p}| \\ \omega_{k,\ell,j,p} &= \tan^{-1} \frac{\Im(w_{k,\ell,j,p})}{\Re(w_{k,\ell,j,p})}, \end{aligned} \quad (\text{A.1})$$

where \Im is the imaginary part and \Re is the real part of the wavelet coefficients, w ;

3. Randomly sort the original elevations to give an initial elevation surface, $z^{(0)}$;
4. Take its two-dimensional DTCWT to derive randomised wavelet phases, $\omega_{k,j}^{(0)}$ for each scale and position;
5. Produce new $w_{k,j}^{(1)}$ by combining the original amplitudes with the randomised phases:

$$w_{k,j}^{(1)} = A_{k,j} \exp(i\omega_{k,j}^{(0)}) \quad (\text{A.2})$$

6. Iterate the following steps until a convergence criterion is met, where at each step, s :
 - (a) Take the inverse DTCWT to give a new DEM, $z^{(s)}(x, y)$ and then apply the amplitude adjustment step where a mapping is established between the original elevations, $z(x, y)$, and the $z^{(s)}(x, y)$ by rank-order matching to permit the values of $z^{(s)}$ to be replaced by the value in $z(x, y)$ with the same rank;
 - (b) Take the DTCWT and obtain the new phases, $\omega_{k,j}^{(s)}$. Combine these with the original amplitudes, $A_{k,j}$ to give the $w_{j,k}^{(s+1)}$ using the s 'th iterated variant of eq. (A.2).

Gradual multifractal reconstruction (GMR) generates synthetic data based on the IAAWT algorithm between limits of $\eta = 0$ (the original IAAWT algorithm) and $\eta = 1$ (the original dataset). Randomization is constrained between these limits to populate the

567 continuum with surrogate data. To do this we first define an energy measure that needs
 568 to account for the decimated nature of the dual tree complex transform by weighting the
 569 coefficients by a factor 2^j (i.e. we adopt an L1 norm):

$$E_\eta = \sum_{j=1}^J \sum_{p=1}^6 \sum_{k=1}^K \sum_{\ell=1}^L \frac{|w_{k,\ell,j,p}|^2}{2^j} \quad (\text{A.3})$$

570 That is, with $j = 1, \dots, J$ scales, there are $K \times L$ coefficients, where $K, L = 2^{J-j}$ in each
 571 of six orientation planes at each scale, meaning that more energy will be associated with
 572 each coefficient on average at the larger j , necessitating the introduction of the denomina-
 573 tor. We then place the absolute values for the $w_{k,\ell,j,p}$ in descending rank order and fix the
 574 first r coefficients such that $\frac{\sum_{r=1}^{K \times N} |w_r|^2}{E_\eta} \geq \eta$. This selected set of coefficients are fixed in
 575 place on the wavelet coefficient template, while the others are phase randomized using eq.
 576 (A.2).

577 Acronyms

578 **DEM** Digital elevation model
 579 **DTCWT** Dual-tree complex wavelet transform
 580 **GMR** Gradual multifractal reconstruction
 581 **GWR** Gradual wavelet reconstruction
 582 **HECAS** Hölder exponent-catchment area scaling
 583 **IAAFT** Iterated amplitude-adjusted Fourier transform
 584 **IAAWT** Iterated amplitude-adjusted wavelet transform
 585 **PDF** Probability distribution function
 586 **RMSE** Root-mean-squared-error
 587 **XLE** Experimental Landscape Evolution

588 Acknowledgments

589 This work was supported by Royal Academy of Engineering/Leverhulme Trust Senior Re-
 590 search Fellowship LTSRF1516-12-89 awarded to the lead author, who was also supported
 591 by Loughborough University's HPC Hydra cluster. Digital elevations for the experimental
 592 data and the sub-regions of the Ochlockonee River basin and Cowlitz River basin used in
 593 this study may be obtained from <http://doi.org/10.5281/zenodo.3922330>.

594 References

595 Ali, N., A. Fuchs, I. Neunaber, J. Peinke, and R. B. Cal (2019), Multi-scale/fractal pro-
 596 cesses in the wake of a wind turbine array boundary layer, *Journal of Turbulence*, 20(2),
 597 93-120.
 598 Arnéodo, A., E. Bacry, S. Jaffard, and J. F. Muzy, (1998), Singularity spectrum of multi-
 599 fractal functions involving oscillating singularities, *J. Fourier Analys. Appl.*, 4, 159-174.
 600 Arrell, K. E., P. F. Fisher, N. J. Tate, and L. Bastin, (2007), A fuzzy c -means classifica-
 601 tion of elevation derivatives to extract the morphometric classification of landforms in
 602 Snowdonia, Wales, *Comp. Geosci.*, 33(10), 1366-1381.
 603 Basu, S., E. Foufoula-Georgiou, B. Lashermes, and A. Arneodo (2007), Estimating in-
 604 termittency exponent in neutrally stratified atmospheric surface layer flows: a robust
 605 framework based on magnitude cumulant and surrogate analyses, *Phys. Fluids*, 19(11),
 606 115102, doi:10.1063/1.2786001.
 607 Benzi, R., L. Biferale, A. Crisanti, G. Paladin, M. Vergassola and A. Vulpiani (1993), A
 608 random process for the construction of multiaffine fields, *Physica D*, 65, 352-358.

- 609 Boon III, J. D. and R. J. Byrne (1981), On basin hypsometry and the morphodynamic
610 response of coastal inlet systems, *Marine Geol.*, *40*, 27-48.
- 611 Brocklehurst, S. H. and K. X. Whipple (2004), Hypsometry of glaciated landscapes, *Earth*
612 *Surf. Proc. Land.*, *29*, 907-926, doi:10.1002/esp.1083.
- 613 Clubb, F. J., S. M. Mudd, D. T. Milodowski, M. D. Hurst, and L. J. Slater (2014), Objec-
614 tive extraction of channel heads from high-resolution topographic data, *Water Resour.*
615 *Res.*, *50*, 4283-4304, doi:10.1002/2013WR015167.
- 616 Echelard, A., J. Lévy Véhel, and A. Philippe (2015), Statistical estimation for a class of
617 self-regulating processes, *Scand. J. Stat.*, *42*(2), 485–503.
- 618 Ehsani, A. H. and F. Quiel (2008), Geomorphometric feature analysis using morphometric
619 parameterization and artificial neural networks, *Geomorphology*, *99*(1-4), 1-12.
- 620 Evans, I. S. and C. J. McLean (1995), The land surface is not unifractal: variograms,
621 cirque scale and allometry, *Zeit. für Geomorph. Suppl.*, *101*, 127-147.
- 622 Frisch, U. and G. Parisi (1985), The singularity structure of fully developed turbulence,
623 in *Turbulence and Predictability in Geophysical Fluid Dynamics and Climate Dynamics*
624 edited by M. Ghil, R. Benzi and G. Parisi, pp.84-88, Elsevier.
- 625 Gagnon, J.-S., S. Lovejoy, and D. Schertzer (2006), Multifractal earth topography, *Nonlin.*
626 *Proc. Geophys.*, *13*(5), 541-570.
- 627 Gasparini, N.M., and K. X. Whipple (2014), Tectonic control of topography, rainfall pat-
628 terns, and erosion during rapid post12 Ma uplift of the Bolivian Andes, *Lithosphere*
629 *6*(4) 251-268, doi:10.1130/L322.1.
- 630 Hack, J. T. (1957), Studies of longitudinal stream profiles in Virginia and Maryland, *U.S.*
631 *Geol. Surv. Prof. Pap.*, *294-B*, 197.
- 632 Jaffard, S. (1997), Multifractal formalism for functions .1. Results valid for all functions,
633 *SIAM J. Math. Anal.*, *28*, 944-970.
- 634 Jerolmack, D.J. and C. Paola (2010), Shredding of environmental signals by sediment
635 transport, *Geophys. Res. Lett.* *37*(19), L19401.
- 636 Keylock, C. J. (2009), Evaluating the dimensionality and significance of active periods in
637 turbulent environmental flows defined using Lipschitz/Hölder regularity, *Environ. Fluid*
638 *Mech.*, *9*, 509-523.
- 639 Keylock, C. J. (2010), Characterizing the structure of nonlinear systems using gradual
640 wavelet reconstruction, *Nonlinear Proc. Geophys.*, *17*, 615–632.
- 641 Keylock, C. J. (2012), A resampling method for generating synthetic hydrological time
642 series with preservation of cross-correlative structure and higher order properties, *Water*
643 *Resour. Res.*, *48*(W12521), doi:10.1029/2012WR011923.
- 644 Keylock, C. J. (2017), Multifractal surrogate-data generation algorithm that preserves
645 pointwise Holder regularity structure, with initial applications to turbulence, *Phys. Rev.*
646 *E*, *95*, 032,123.
- 647 Keylock, C. J. (2018), Gradual multifractal reconstruction of time-series: Formulation of
648 the method and an application to the coupling between stock market indices and their
649 Hölder exponents, *Physica D*, *368*, 1–9.
- 650 Keylock, C. J. (2019), Hypothesis testing for nonlinear phenomena in the geosciences us-
651 ing synthetic, surrogate data, *Earth Space Sci.*, *6*, doi: 10.1029/2018EA000435.
- 652 Keylock, C. J., M. Ghisalberti, G. G. Katul, and H. M. Nepf (2020a), A joint velocity–
653 intermittency analysis reveals similarity in the vertical structure of atmospheric and hy-
654 drospheric canopy turbulence, *Env. Fluid Mech.*, *20*, 77-101, doi:10.1007/s10652-019-
655 09694-w.
- 656 Keylock, C. J., K. Nishimura and J. Peinke (2012), A classification scheme for turbu-
657 lence based on the velocity-intermittency structure with an application to near-wall
658 flow and with implications for bedload transport, *J. Geophys. Res.*, *117*, F01037, doi:
659 10.1029/2011JF002127.
- 660 Keylock, C. J., A. Singh, and E. Foufoula-Georgiou (2014b), The complexity of gravel-bed
661 river topography examined with gradual wavelet reconstruction, *J. Geophys. Res.*, *119*,
662 682–700, doi:10.1002/2013JF002999.

- 663 Keylock, C. J., A. Singh, P. Passalacqua and E. Foufoula-Georgiou (2020b), Hölder-
 664 conditioned hypsometry: A refinement to a classical approach for the characterization
 665 of topography, *Water Resour. Res.*
- 666 Keylock, C. J., R. Stresing, and J. Peinke (2015) Gradual wavelet reconstruction of the
 667 velocity increments for turbulent wakes, *Phys. Fluids*, 27, art. no. 025104.
- 668 Kingsbury, N. (2001), Complex wavelets for shift invariant analysis and filtering of sig-
 669 nals, *Appl. Comput. Harmon. Anal.*, 10, 234–253.
- 670 Klinkenberg, B., and M. F. Goodchild (1992), The fractal properties of topography: A
 671 comparison of methods, *Earth Surf. Proc. Land.*, 17(3), 217-234.
- 672 Kolmogorov, A. N. (1941), The local structure of turbulence in incompressible viscous
 673 fluid for very large Reynolds numbers, *Dokl. Akad. Nauk. SSSR.*, 30, 299-303.
- 674 Lague, D. and P. Davy (2003), Constraints on the long-term colluvial erosion law by an-
 675 alyzing slope-area relationships at various uplift rates in the Siwaliks Hills (Nepal), *J.*
 676 *Geophys. Res.*, 108(2), ETG 8-1 - ETG 18-11.
- 677 Lavallée, D., S. Lovejoy, D. Schertzer, and P. Ladoy (1993), Nonlinear variability of land-
 678 scape topography: multifractal analysis and simulation, in De Cola, L. and N. Lam,
 679 *Fractals in Geography*, p. 171-205, Prentice-Hall, Englewood, N.J.
- 680 Lévy Véhel, J. (2013), Beyond multifractional Brownian motion: New stochastic models
 681 for geophysical modelling, *Nonlin. Proc. Geophys.*, 20(5), 643–655.
- 682 Lifton, N. A., and C. G. Chase (1992), Tectonic, climatic and lithologic influences on
 683 landscape fractal dimension and hypsometry: implications for landscape evolution in
 684 the San Gabriel Mountains, California, *Geomorphology*, 5(1-2), 77-114.
- 685 Mandelbrot, B. and J. W. van Ness (1968), Fractional Brownian motions, fractional noises
 686 and applications, *SIAM Review*, 10, 4, 422-437.
- 687 Outcalt, S.I. and M. A. Melton (1992), Geomorphic application of the Hausdorff-Besi-
 688 covich dimension, *Earth Surface Processes and Landforms* 17(8), 775-787.
- 689 Passalacqua, P., T. Do Trung, E. Foufoula-Georgiou, G. Sapiro, and W. E. Dietrich (2010),
 690 A geometric framework for channel network extraction from lidar: Nonlinear diffusion
 691 and geodesic paths, *J. Geophys. Res.*, 115 (1), F01002.
- 692 Peltier, R. F. and J. Lévy Véhel (1995), Multifractal Brownian motion: definition and
 693 preliminary results, *INRIA Tech. Report 2645*.
- 694 Perron, J. T., J. W. Kirchner, and W. E. Dietrich (2008), Spectral signatures of characteris-
 695 tic spatial scales and nonfractal structure in landscapes, *J. Geophys. Res.*, 113(F04003),
 696 doi:10.1029/2007JF000866.
- 697 Poggi, D., A. Porporato, L. Ridolfi, J. D. Albertson, and G. G. Katul (2004), Interaction
 698 between large and small scales in the canopy sublayer, *Geophys. Res. Lett.*, 32(L05102),
 699 10.1029/2003GL018611.
- 700 Rodriguez-Iturbe, I., and A. Rinaldo (1997), *Fractal River Basins: Chance and Self-*
 701 *Organization*, Cambridge Univ. Press, New York.
- 702 Schreiber, T., and A. Schmitz (1996), Improved surrogate data for nonlinearity tests, *Phys.*
 703 *Rev. Lett.*, 77, 635–638.
- 704 Schwenk, J., and E. Foufoula-Georgiou (2017), Are process nonlinearities encoded
 705 in meandering river planform morphology?, *J. Geophys. Res. Earth Surf.*, 122,
 706 doi:10.1002/2016JF003,929.
- 707 Selesnick, I. (2002), The design of approximate Hilbert transform pairs of wavelet bases,
 708 *IEEE Trans. Sig. Proc.*, 50, 1144–1152.
- 709 Selesnick, I., R. Baraniuk, and N. Kingsbury (2005), The dual-tree complex wavelet trans-
 710 form, *IEEE Signal Proc. Mag.*, 22, 123.
- 711 Seuret, S. and J. Lévy Véhel (2003), A time domain characterization of 2-microlocal
 712 spaces, *J. Fourier Anal. Appl.*, 9, 473-495.
- 713 Singh, A., L. Reinhardt, and E. Foufoula-Georgiou (2015), Landscape reorganization under
 714 changing climatic forcing: Results from an experimental landscape, *Water Resour. Res.*,
 715 51, 4320-4337, doi:10.1002/2015WR017161.

- 716 Strahler, A. N. (1952), Hypsometric (area-altitude) analysis of erosional topography, *Geol.*
717 *Soc. Am. Bull.*, *63*, 1117-1142.
- 718 Tejedor, A., A. Singh, I. Zaliapin, A. L. Densmore, and E. Foufoula-Georgiou (2017),
719 Scale-dependent erosional patterns in steady-state and transient-state landscapes, *Sci.*
720 *Adv.*, *3*, e1701683.
- 721 Theiler, J., S. Eubank, A. Longtin, B. Galdrikian, and J. Farmer (1992), Testing for non-
722 linearity in time series: the method of surrogate data, *Physica D*, *58*, 77–94.
- 723 Tokunaga, E. (1978), Consideration on the composition of drainage networks and their
724 evolution, *Tokyo Metro. Univ., Japan, Geograph. Rep.*, *13*, 1-27.
- 725 Venema, V., S. Meyer, S. G. Garcia, A. Kniffka, C. Simmer, S. Crewell et al. (2006), Sur-
726rogate cloud fields generated with the iterative amplitude adapted Fourier transform al-
727gorithm, *Tellus A*, *58*, 104-120.
- 728 Veneziano, D. and V. Iacobellis (1999), Self-similarity and multifractality of topographic
729 surfaces at basin and subbasin scales, *J. Geophys. Res.* *104*(B6), 12797-12812.
- 730 Venugopal, V., S. Roux, E. Foufoula-Georgiou, and A. Arneodo (2006), Revisiting mul-
731tifractality of high-resolution temporal rainfall using a wavelet-based formalism, *Water*
732 *Resour. Res.* *42*(W06D14), doi:10.1029/2005WR004489.
- 733 Willgoose, G. (1994), A statistic for testing the elevation characteristics of landscape sim-
734 ulation models, *J. Geophys. Res.*, *99*(B7), 13987-13996, doi:10.1029/94JB00123.
- 735 Zanardo, S., I. Zaliapin, and E. Foufoula-Georgiou (2013), Are American rivers Tokunaga
736 self-similar? New results on fluvial network topology and its climatic dependence, *J.*
737 *Geophys. Res.: Earth Surf.*, *118*, 1-18, doi:10.1002/jgrf.20029.